MTLA 45 (2026) 102648

Contents lists available at ScienceDirect

Materialia

journal homepage: www.elsevier.com/locate/mtla

Full Length Article

Residual stress in Germanium single crystals caused by femtosecond laser micromachining

R. Fréville [a,*], P.A. Gruber [a], S. Lee [a], J.S. Micha [b], O. Robach [b], O. Ulrich [b], C. Kirchlechner [a]

[a] Karlsruhe Institute of Technology, Institute for Applied Materials, P.O. Box 3640 76021, Karlsruhe, Germany
[b] Université Grenoble Alpes, CEA-Grenoble/Institut de Recherche Interdisciplinaire de Grenoble 38000, Grenoble, France

ARTICLE INFO

Keywords:
Synchrotron
Laue-microdiffraction: Digital image correlation
Residual stress
femtosecond laser
metal
focused ion beam

ABSTRACT

Femtosecond laser (fs-laser) milling has emerged as a promising technique for high-precision material processing, offering significantly faster ablation rates compared to Ga^+ Focused Ion Beam (FIB) milling. While fs-laser ablation is often considered to be athermal, its impact on surface features, such as redeposited material, raises concerns about its influence on microstructure and residual stress fields. This study explores the mechanical effects of fs-laser and FIB milling on a germanium single crystal, using synchrotron-based Laue microdiffraction coupled with Digital Image Correlation to characterize induced residual stresses and their spatial distribution. The further development of this technique allows to push the strain resolution to 10^{-5}, which enabled a clear identification of the influence of the redeposition structure.

1. Introduction

Femtosecond laser (fs-laser) cutting has seen significant advancements in material processing applications [1–3]. Offering ablation rates several orders of magnitude higher than Focused Ion Beam (FIB) milling [4,5], fs-lasers are often considered athermal due to their ultra-short pulse durations, which minimize bulk thermal effects [6]. However, fs-laser ablation introduces unique surface features, such as laser-induced periodic surface structures (LIPSS) [7,8], and can lead to the formation of redeposited material [5], which may obscure microstructural features or alter mechanical properties. This raises the critical question of how fs-laser machining impacts the underlying material, particularly in terms of thermal and mechanical effects.

The thermal impact of fs-laser ablation has been examined using characterization methods like scanning electron microscopy (SEM) [9–11] for surface defect analysis and transmission electron microscopy (TEM) [9,12–16], which has revealed dislocation damage extending from nanometer depths to as much as 5 μm. Mechanical property investigations, such as those by Gigax et al [17], demonstrated that removing 5 μm from the laser-affected surface can restore comparable compression behavior between FIB-milled and fs-laser-milled micropillars in copper. Additionally, Borowiec et al [14] employed degree-of-polarization (DOP) analysis to detect residual stresses extending up to 20 μm from the fs-laser cut in semiconductors, achieving a strain resolution of 10^{-4} and a spatial resolution of 1 μm.

FIB milling remains a cornerstone for micromechanical sample preparation due to its precision in shaping metallographic surfaces. However, ion bombardment during FIB processing can introduce microstructural defects, as reviewed by Borasi et al [18], motivating the search for complementary or alternative methods such as plasma FIB or fs-laser milling [4]. The integration of these techniques could enhance sample preparation workflows by mitigating damage while maintaining efficiency.

Several techniques exist to characterize residual stresses, including X-ray diffraction (XRD), neutron diffraction, or Raman spectroscopy. However, these methods often lack either for spatial resolution or sensitivity to local variations at the micrometre scale. In this context, synchrotron-based Laue microdiffraction (μLaue) has emerged as an invaluable tool to measure the deviatoric strain tensor.

This non-destructive method offers strain resolution of 10^{-4} and spatial resolution of 1 μm [19,20]. μLaue diffraction patterns, consisting of shifted Laue peaks, are sensitive to lattice distortions and crystal rotations, providing insight into the stress distribution within the material [21,22].

In this study, we present an investigation into the effects of fs-laser and FIB milling on residual stresses in a germanium single crystal,

* Corresponding author.
E-mail address: freville.rob@gmail.com (R. Fréville).

https://doi.org/10.1016/j.mtla.2025.102648
Received 18 September 2025; Accepted 23 December 2025
Available online 24 December 2025

enabled by the unique combination of μLaue diffraction and digital image correlation (DIC). To achieve this, we developed specific experimental protocols to ensure precise stress characterization. We also explored, for the first time in this context, the potential influence of a redeposition structure with respect to different laser parameters. These methodological advances provide new insights into stress evolution in laser- and FIB-processed germanium, paving the way for improved micromachining strategies.

2. Methods

2.1. Sample preparation

A Germanium wafer with [110] out of plane orientation was used to mill two triangles using a fs-laser (Crossbeam 550 L, Zeiss). Scanning Electron Microscope (SEM) images corresponding to the two triangles were taken in the same microscope with an acceleration voltage of 5 kV and are presented in Fig. 1. The laser parameters used to make the patterns are summarized in Table 1. In both cases, the fluence was about 0.07 J/cm^2, with a spot size of 14 μm [4]. Rotation of the direction of milling are done after each milling step in order to reduce directional artifact, and distribute heat and energy more evenly. The two triangles have similar geometry: each part is a rectangle with dimensions ~260 μm x 65 μm, and the angle between two rectangles is 60 ° Finally, the distance between T1 and T2 is ~570 μm, which ensure that there is no mutual influence of the two triangles.

In addition to this first fs-laser based milling process, some parts at the edges of the triangles (see arrows in Fig. 1) were further cut via Ga^+ FIB, with three successive steps: (1) a current probe of 15 nA and a dose of 1000 mC/cm^2, (2) 3 nA and 200 mC/cm^2, (3) 1.5 nA and 200 mC/cm^2 in order to produce a sharp Ge edge. The two distinct parts (only fs-laser and FIB+fs-laser) will allow the comparison between the two triangle processes presented in term of residual stresses for instance.

2.2. Laue microdiffraction

The diffraction experiment was carried out at the CRG-IF beamline (BM32) of the European Synchrotron Radiation Facility (ESRF, France). The exact experimental setup is described in Refs [22,23]. Samples were scanned using a polychromatic beam (5–23 keV) of 0.7 × 0.8 μm^2 full width at half maximum (FWHM) in reflection geometry with a sample tilt of 40°. The Laue diffraction patterns were collected using a Photonic Sciences sCMOS detector located above the sample (2θ = 90 °). The sample to detector distance was around ~77.1 mm. The exact detector position and orientation with respect to sample position and incoming beam orientation were calibrated directly on the sample using an unstrained part of the sample (Ge wafer with [110] out of plane orientation) to increase accuracy. The sample was placed into the focused beam using an optical microscope normal to the sample surface. With the beam position being constant in space, diffraction Laue patterns are obtained by simple translation motions of the sample in front of the beam.

For each triangle, two scans were performed: a large mapping of the sample covering an area of 280 × 300 μm^2 with a 4 μm resolution in both directions, resulting in a total of 5 396 diffraction patterns; and a zoom in the lower part of the triangle covering an area of 140 × 70 μm^2 with a resolution of 1 μm in both directions, resulting in a total of 10 011 diffractions patterns.

Table 1
Parameters used to mill the two triangles using the fs-laser. In both cases, the fluence was about 0.07 J/cm^2.

Name	Number of repeats	Speed (mm/s)	Frequency (kHz)	Depth (μm)	Rotation after repeat
T1	5	50	20	20	180 °
T2	100	10	10	50	37 °

2.3. Analysis of Laue patterns with Laue-Dic

The standard procedure to estimate elastic strain from Laue patterns is divided in two steps. First, the setup is calibrated (sample to detector position and orientation of the beam) with a well-known and strain-free sample. Then, using the same geometrical setup, the Laue pattern are recorded for the sample of interest. Positions of Laue spots on the two-dimensional detector are estimated by fitting individual diffraction peaks with a standard analytical function (a Gaussian shape in the present case). Diffraction spots are attributed to a specific orientation based on the distance between the centre of the diffraction peaks. The deviation from the theoretical unstrained configuration allows to compute strain. Calibration and processing of data were then performed using the LaueTools software [24] using the procedure described above. The treatment performed on each image is independent. Doing so, the obtained strain resolution is given with a precision of about 10^{-4} [25].

In addition, in the present case (see Fig. 2), the diffraction peaks remain circular at every position. It is then possible to reach an even higher strain resolution as the conservation of the global peak shape

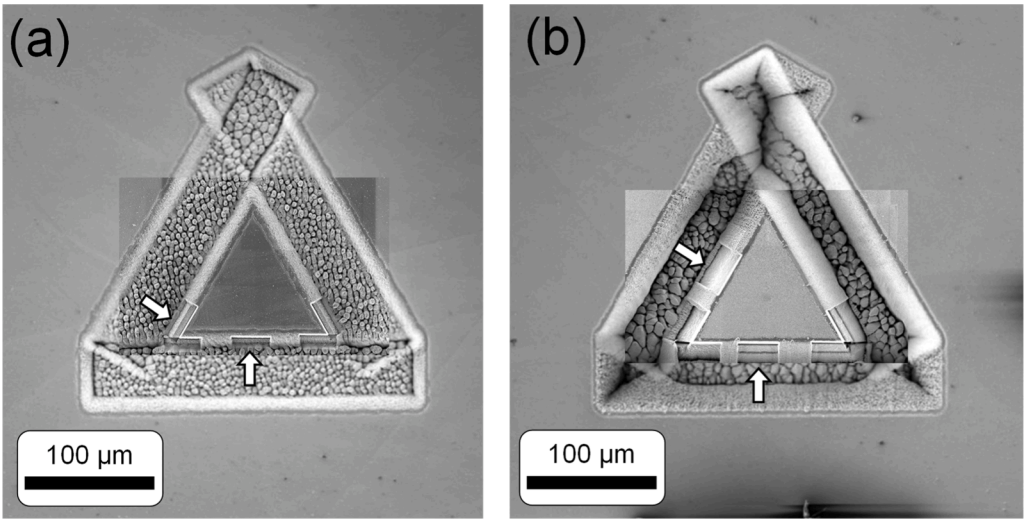

Fig. 1. Composite SEM images of the triangles cut in the Ge wafer. General overview of the triangle T1 (a) and T2 (b) cut with the parameters given in Table 1. Additional FIB cut was performed on the edges of the inner triangle (see arrows and text for further information).

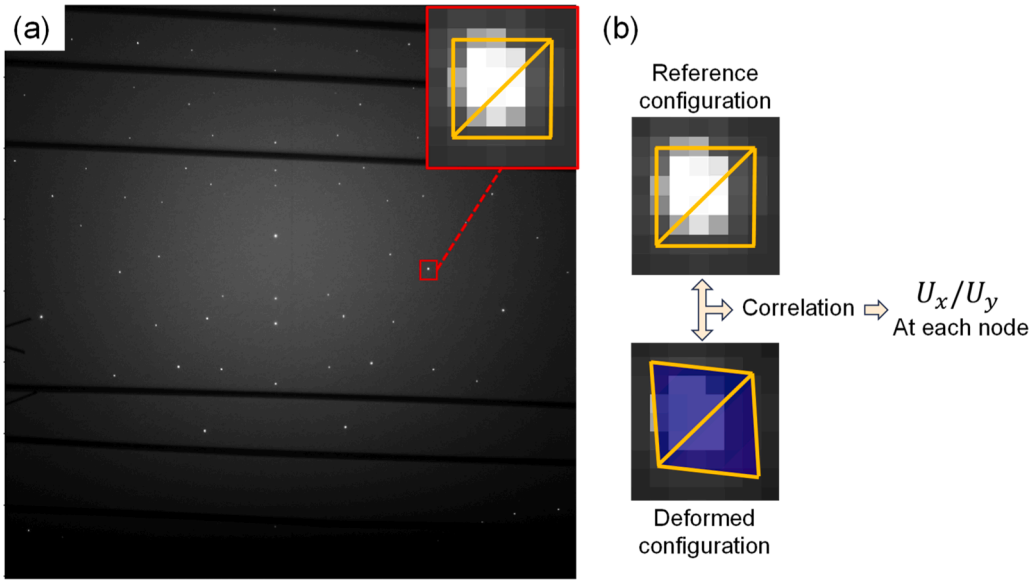

Fig. 2. (a) Typical Laue pattern recorded on the Germanium wafer. The diffraction peaks have a circular shape. Inset: zoom on one diffraction peak with the correlation window used for Laue-DIC. In yellow are highlighted the two triangles used to obtain peak displacements. **(b) Schematic representation of the correlation procedure.** The correlation is based on the conservation of gray levels. Displacements in the plane (U_x, U_y) are obtained at each node of the mesh.

allows for the implementation of the so-called Laue-DIC [25–28], based directly on digital image correlation. According to previous studies [26, 29], the strain resolution with Laue-DIC is given with a precision of about 10^{-5}. The implementation of Laue DIC and improvement in strain resolution were a requisite to be able to resolve completely the deviatoric strain evolution in the proposed experiment.

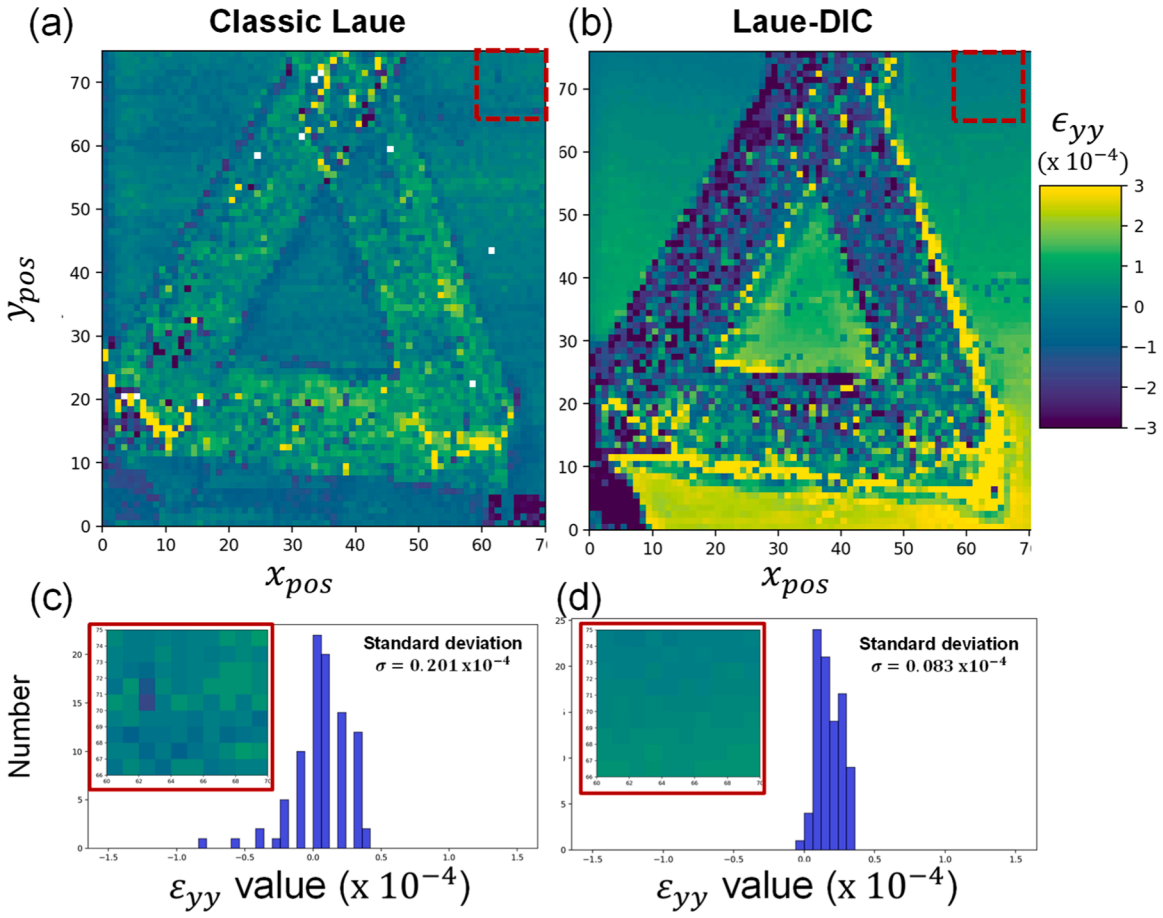

Fig. 3. Comparison of the obtained resolution between the two methods. Colormaps for the strain component ε_{yy} obtained with (a) classical Laue treatment and (b) Laue-DIC for the first triangle T1. More details of the strain evolution can be observed with Laue-DIC due to the lower noise. (c) & (d) Zoom at the location of the red squares in (a) & (b) and the histogram of strain associated to this area.

A second data processing was then performed with Laue-DIC. The diffracted Laue pattern can directly be used here, no artificial pattern is needed to perform the correlation. Instead, the correlation is performed in boxes around each diffraction peak as described in [27] and schematically represented in Fig. 2. The correlation is then performed between one configuration of reference (in that case unstrained Ge outside of the cutting part) and every point of the scanned area. Displacements in the detector plane are computed for each diffraction peak and deviatoric strains are derived from these displacements [28].

The optical flow problem was solved with the UFreckles software [30]. It relies on a global approach in which displacements are discretized on a finite element basis. A mesh of two linear triangle elements was used for each diffraction peak. The size of correlation windows was adapted to each diffraction peaks to avoid taking too much background noise (variable due to synchrotron radiation) into account. Each part of the mesh includes 8–10 pixels from the detector. The correlation routine integrated a Tikhonov regularization, with a cut-off wavelength in the same order as the mesh size. Around 50 diffraction peaks are considered to increase accuracy (same order of magnitude as classic-Laue). The final error was estimated with the value of deviatoric strain found in the 5 scanned points around the position of the calibration; all the points are supposed to be part of unstrained Germanium. The strain component values are then given with an estimated error of $4.8\text{x}10^{-6}$.

In Fig. 3, a comparison of the two methods in analysing the strain in ε_{yy} is shown for the first triangle. In particular, the histograms of strain distribution in a homogeneous region have been plotted for both treatments (Fig. 3-(c-d)). The spread is much lower with Laue-DIC compared to classic Laue treatment, with a factor of 5 between the two calculated standard deviations. Laue-DIC treatment also exhibits less scatter, visible as reduced background noise (compare Fig. 3a and b).

2.4. Computation of stress

To study the possible impact of fs-laser and/or FIB on residual stresses, the stress components were estimated from the measured strain using the Hooke's law:

$$[\sigma] = [C].[\varepsilon] \quad (1)$$

where C is the stiffness tensor of Ge with the elastic constant $C_{11} = 129.8$ GPa, $C_{12} = 48.8$ GPa, and $C_{44} = 67.3$ GPa [31] for a crystal with out of plane direction [001]. To take into account the difference of out of plane direction, a rotation of the stiffness tensor has been performed. Laue diffraction experiments without measuring the energy of a Laue spot can only be used to compute the deviatoric strain tensor. With the safe assumption that the out-of-plane component σ_{zz} is zero at the surface, the complete stress tensor can be computed. We think this assumption holds for the top surface of the inner triangle, which has not been irradiated directly by the fs-laser. In the following, we will only discuss the evolution of stresses and strains in the interior of the triangle.

3. Tilt correction

The Ge wafer was glued to the sample holder, which caused a slight tilt. Given the large scan area exceeding 300 μm, this tilt needs to be taken into account for the calibration of the sample-detector distance.

The misalignment of the sample can be evidenced in Fig. 3-(a)-(b) with the systematic variation of the computed strain. Indeed, one would expect to be in an unstrained region of Ge outside the triangle, and consequently have a uniform colour map, e.g. at the right border of Fig. 3-(b). To check the misalignment hypothesis caused by gluing of the sample to the stage, we compared two Laue-DIC analysis with the reference image located respectively in the top part ($x_{pos} = 70$, $y_{pos} = 73$) and in the middle ($x_{pos} = 70$, $y_{pos} = 35$). Fig. 4 displays the evolution of strain components (ε_{xx}, ε_{yy} and ε_{zz}) along a vertical line at $x_{pos} = 70$ in the two mentioned cases: reference image on top (a) and in the middle (b). Observations are similar for the three other components. In all cases, a linear evolution is found. The slopes are the same (-0.0344 for ε_{yy} in mid, and -0.0347 for ε_{yy} in top for instance). Only a shift due to the position where the reference image is taken is visible. This is in line with the hypothesis of a tilt during mounting on the sample holder.

A tilt correction is then performed on each component so that a strain free region is obtained around the triangle. The correction consists of a linear shift of each component based on the slope obtained along the vertical line at $x_{pos} = 70$ (see Fig. 4-(a)) for the vertical tilt. It corresponds to a tilt misalignment of 4.6° during mounting of the sample. A minor correction for the horizontal tilt is also performed with the same procedure. The corresponding maps for all the 6 components before and after correction for T1 are displayed in the Supplementary material. It has to be noted that we used the same correction for the two triangles, and that all results presented after are obtained with this correction on Laue-DIC analysis and a configuration of reference located on top of the sample.

4. Estimation of the area impacted by the fs-laser

4.1. Evolution of stress components inside the triangle

The changes of residual stress at the edge of the triangles caused by the fs-laser were analysed based on the high-resolution scan of the lower edge. For instance, the σ_{xx} in-plane component obtained for the triangle T1 is displayed as colormap in Fig. 5, together with the evolution of stress components along two distinct vertical lines: one across the part only cut with the fs-laser (black line), and one with both fs-laser and FIB (white line). Both lines start at the experimentally determined position

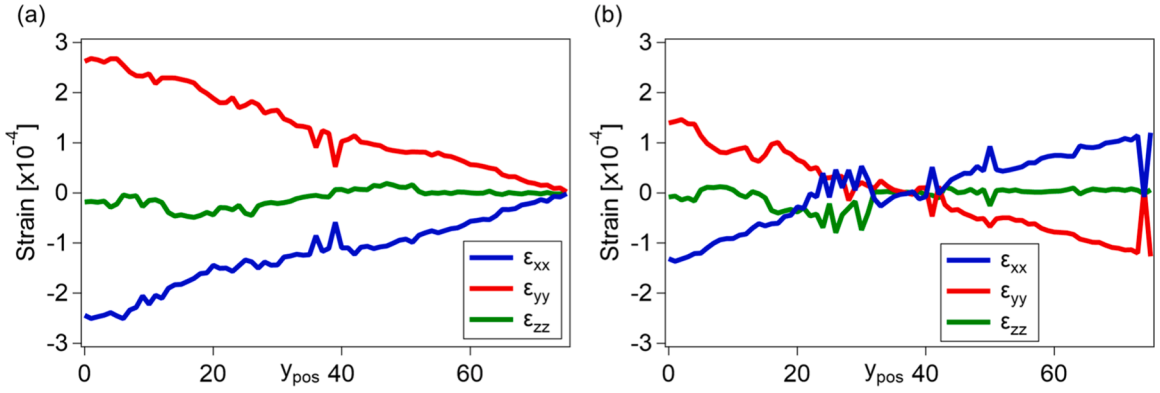

Fig. 4. Evidence of a tilt during mounting on the sample holder. Evolution of the three strain components ε_{xx} (blue), ε_{yy} (red), and ε_{zz} (green) along a vertical line obtained for two analyses with Laue-DIC with reference image taken (a) at the top, and (b) in the middle. The slopes are identical, only a shift due to the location of reference image is observed, which is in line with existence of an artificial tilt.

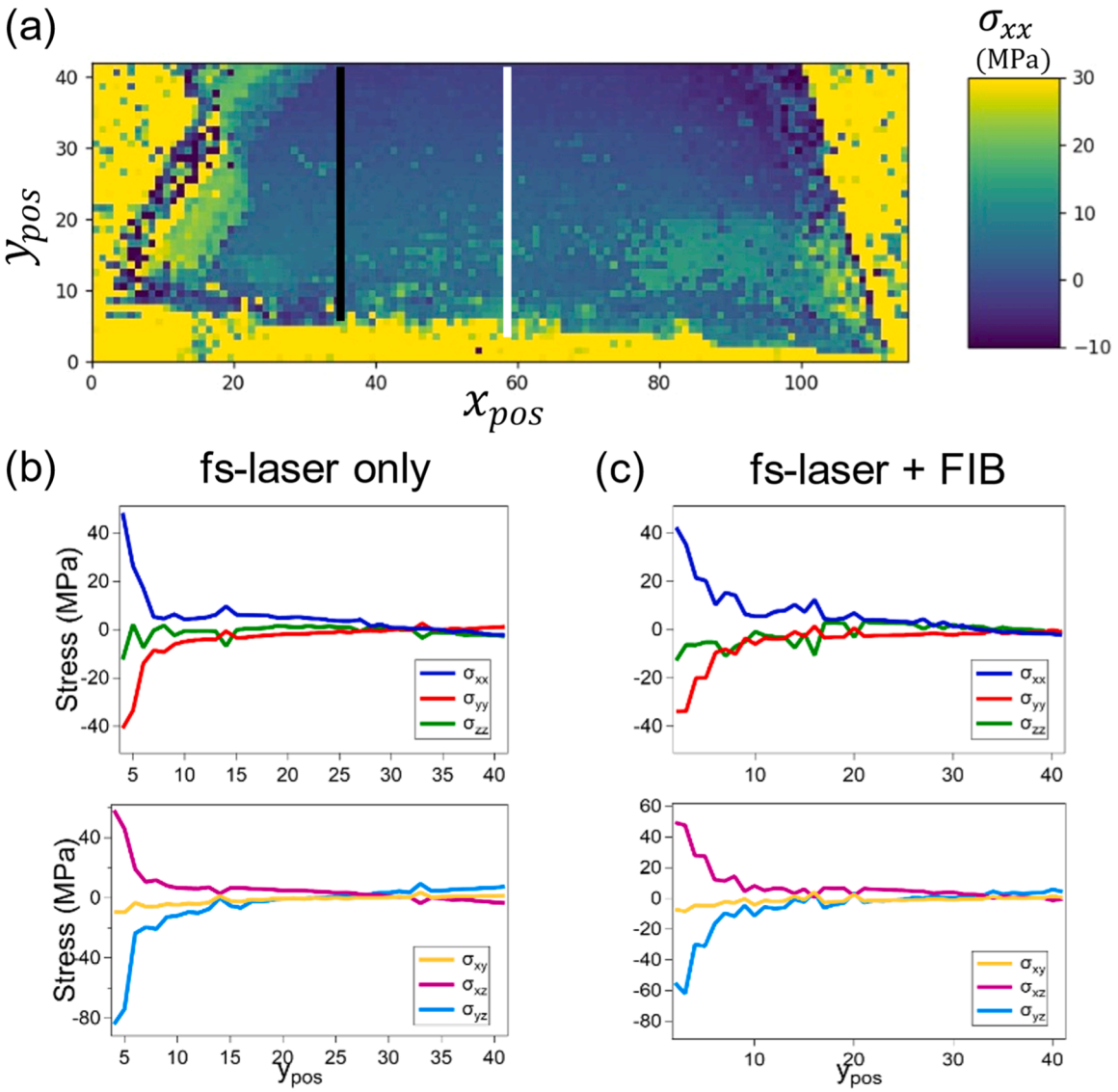

Fig. 5. Evolution of stress components inside the triangle T1. (a) colormap of the evolution of the in-plane component σ_{xx} in the centre part. The edges of the triangles can be well determined. The black (resp. white) vertical line indicates the position taken for the stress components evolution displayed in (b), i.e. across the part cut only with fs-laser (resp. (c), i.e. across the part cut with FIB+fs-laser). The top panel displays normal components. The bottom one displays shear components. Evolutions start at the estimated position of the edge (see Supplementary B).

of the edge of the triangle, which is slightly inclined along x direction.

Apart from σ_{zz}, which is equal to zero due to the current experiment's geometry, and σ_{xy}, which is close to zero in the present case, the other stress components present a similar evolution in both cases. No distinction seems to appear between fs-laser and FIB for T1. The evolution can be fitted with an exponential and a linear part as follow:

$$\sigma_{ij} = A\ exp\left(-\frac{y_{pos}}{B}\right) + C\ y_{pos} + D \tag{2}$$

where A, B, C and D are constants to be fitted for each component. For an exponential, 95 % of the decrease appears within 3xB. To evaluate the impacted area, with non-zero residual stresses, the idea is consequently to fit each component with a function as in Eq. (2) and then to define 3B as the limit of the impacted area.

4.2. Results for the first triangle T1

The forementioned procedure was applied to the three sides of T1. For left and right edges, we used horizontal lines with similar strain evolution as presented in Fig. 5. Plots for these edges are reported in the Supplementary material. In each case, a mean of 3 pixels (3 μm) is used to reduce noise from analysis. As σ_{zz} and σ_{xy} are almost zero, these components have not been considered for fitting. We limited the study to the region in the center of the triangle, i.e. at x_{pos} ranging from 25–85 μm. The remaining parts are too close to the corners and therefore would be impacted by the second edge.

The distance from the estimated edge of the triangle to the unaffected region (equals 3B) are displayed in Fig. 6-(a). For fitting, we considered only the part without the plateau mentioned earlier. The edge position itself was determined using the number of indexed spots, which drastically increases once the beam is landing on the inner triangle. The corresponding maps and equation for the bottom edge are displayed in the Supplementary material. In every case, the four components show the same tendency with similar values, documenting that the affected zone is independent of the analysed stress component. Errors in the fit were also computed and are below 1 μm and global error range is determined from the mean dispersion of the four stress components. Within errors bars, no distinction between fs-laser only and FIB + fs-laser is detected. The unaffected region's start lies between 2 and 4

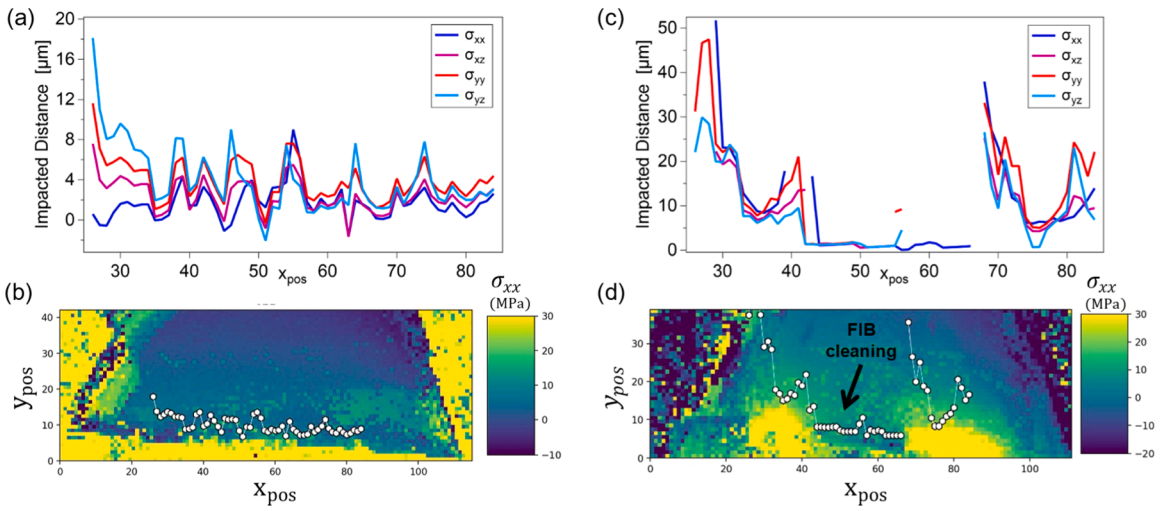

Fig. 6. Determination of the impacted area for T1 and T2. (a) & (c) Results for the individual fitting of the 4 stress components for respectively T1 and T2. The value plotted is the distance to the bottom edge. All 4 components present similar results and almost a constant value can be determined. (b) & (d) Colormap of the evolution of σ_{xx} in the centre part of the triangle, together with the determined of impacted area for respectively T1 and T2. Above the white pentagon lines, it is reasonable to assume a stress-free sample.

µm from the edge, i.e. residual stresses can be seen up to 4 µm above the edge. The boundary is highlighted in Fig. 6–(b) as white dots.

4.3. *Results for the second triangle T2*

A similar analysis was performed on the second triangle, but only on the bottom edge, limited to the positions in the center with x_{pos} ranging from 25–85 µm. Note that between 25 and 30 µm, the stress field may be already impacted by the left edge. This was kept here as an indication to compare qualitatively with the 68–80 µm part. We used the same four stress components for the analysis. Results of fits are displayed in Fig. 6-(c), in the same way as for the first triangle. For a few points, it was not possible to fit the one or two stress components (due to the noise). These points have been removed leading to some discontinuity in Fig. 6-(c). The corresponding maps and equation for the bottom edge are displayed in the Supplementary material. Once again, one can notice that stress components present the same tendency with similar values. For this triangle, a clear distinction between the fs-laser only and FIB + fs-laser parts can be evidenced, as presented in Fig. 6-(d). FIB seems to have a "cleaning" effect to reduce residual stresses. Apart from the border between the two parts, two behaviours are observed: for the part with only fs-laser, unaffected region's start lies between 8 and 13 µm, while it lies at maximum 2 µm for the part further milled with FIB. A strong border effect between the two mentioned parts has to be noted: we observe a discrete jump in the impacted area at x_{pos} of 25, 40, 68. These three locations correspond to the edge between FIB and non-FIB parts (see Fig. 1-(d)).

5. Discussion

There are at least two possible origins of residual stresses. First, the stresses could be attributed to the formation of dislocations inside the sample during the fs-laser milling process. µLaue diffraction can resolve geometrically necessary dislocation through the diffraction peak shape (elongation in one or multiple direction) [32,33]. However, in the present case, and as presented in the Fig. 2, the diffraction peaks remained completely circular with no detectable elongation due to dislocation storage.

A second possibility is the existence of a redeposition structure produced during fs-laser milling. This redeposition structure can build-up stresses during growth as it is well-known from thin film growth processes [34,35], causing the substrate to be strained as well. Consequently, residual stresses are formed in the bulk material close to the redeposition structure. Fig. 7 displays SEM images of the two triangles. Along the border of the fs-laser cut, a clear redeposition structure is observed. Two main differences from the two triangles are evident: (1) the redeposition structure appears denser and thicker for T2 compared to T1; (2) the FIB cut removed apparently all the redeposition structure in T2, while there is still some remaining for T1.

The difference between the density of redeposition structures is attributed to the different laser parameters used during this experiment (see Table 1). In particular, scan speed, repetition rate and the number of repeats may have a crucial role in controlling material redeposition. At low scanning speeds combined with deep passes and a high number of repetitions, the laser repeatedly interacts with the same area generating substantial material in a confined zone and increasing debris redeposition on the surface [36–40]. These observations are in line with the current experiment as more redeposition is observed for the triangle T2 milled with lower speed, higher number of repeat and with deeper passes compared to triangle T1. However, since also the depth of the trench in T2 is significantly deeper than in T1, which is increasing the likelihood of redeposition for geometric reasons in T2, a fair comparison of the two laser parameters is neither possible, nor was it the scope of this work. Nevertheless, a comparison between impacted area in both triangles (see Fig. 6) suggests that the impacted area depends on the amount of redeposition structure produced during the cutting process.

As mentioned earlier, in Fig. 7-(a), a redeposition structure is still visible even after a FIB cut, whereas it is not the case in Fig. 7-(b). All along the edge of the triangle, a constant size of redeposition structure is observed. This is in line with the impacted area determined through µLaue analysis. In the second case, the complete absence of redeposition structure after FIB cut create the so-called "FIB cleaning" effect visible in Fig. 6-(d). In addition, a certain periodicity (around 7 µm for T1 and 9 µm for T2) in the mentioned redeposition is observed. While the precise origin of this structure remains unknown from a laser's parameter perspective, the period would align well (within margin errors) with the oscillations in Fig. 6-(a) and (c), respectively 9 µm for T1 and 12 µm for T2.

These observations point to a clear impact of the redeposition structure. To further check, we compared the experimental stress evolution with theoretical simulation deviated from literature [36]. The exponential decay model has proven effective in describing stress depth distributions in the context of residual stress analysis. Meixner et al [41] demonstrated the validity of this model using diffraction analysis of

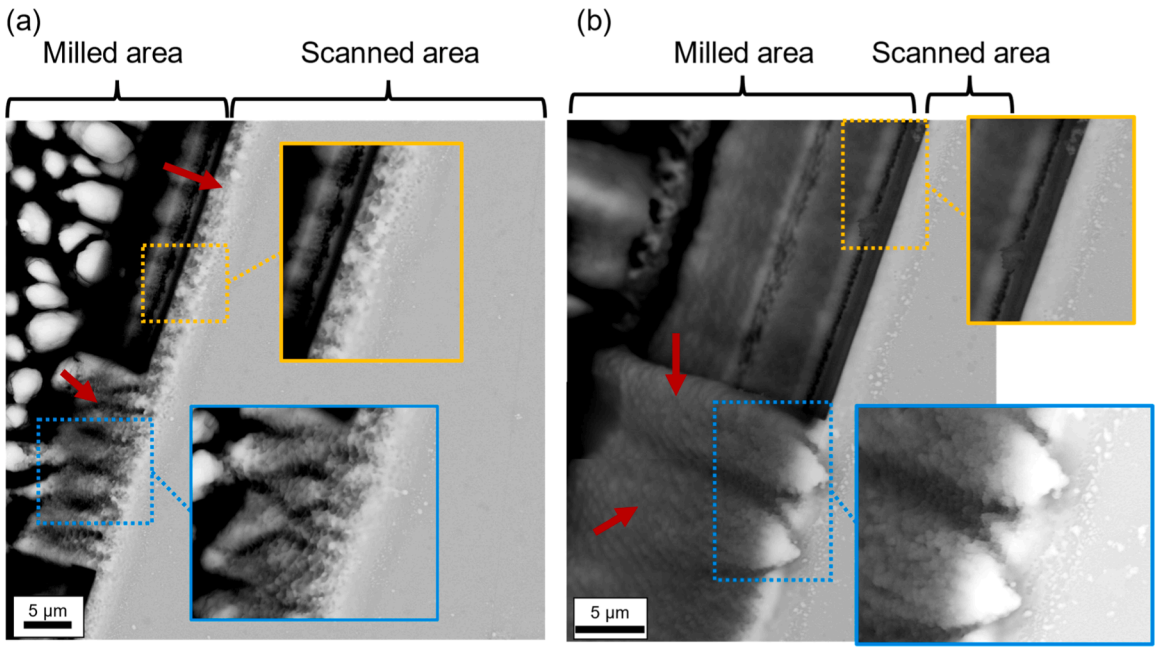

Fig. 7. Redeposition structure due to fs-laser milling, for triangle T1 (a), and T2 (b). The orange boxes (resp. blue boxes) display zooms on the part further cut with FIB (resp. fs-laser only). A clear redeposition structure is evidenced with red arrows. The milled area correspond to the are not taken into account during analysis.

strongly inhomogeneous residual stress depth distributions. By modifying the stress scanning method, they provided experimental evidence aligning with the exponential stress decay observed. Similarly, Stefenelli et al [42] explored the distribution of residual stresses in thin films. Their results showed that stress profiles closely followed an exponential decay, further confirming the model's applicability due to the analogy made between thin films and a redeposition structure. These studies support the hypothesis made of an exponential decay model to describe the evolution of residual stresses due to a redeposition structure.

Consequently, while we do not see any evidence of a modification of the defect structure of germanium by fs-laser ablation within the resolution limits of Laue microdiffraction, we do see the formation of a redeposition structure which causes residual stress also in the region not touched by the fs-laser. Thus, care should be taken when using ablation processes with high sputter yield, because – dependent on the geometry – they might result in redeposition structures and the build-up of residual stress changing materials mechanical and functional properties. It has to be noted, that the parameters used here were not optimized for the material and that an optimization procedure could reduce the amount of redeposition structure created during ablation.

6. Conclusion

We presented here a µLaue-DIC experiment coupled with DIC to study the possible impact of fs-laser and FIB on residual stresses during machining of a germanium sample. The use of DIC improves the strain resolution obtained by an order of magnitude compared to the classical treatment, which is key to perform an in-depth analysis of residual stresses caused by fs-laser ablation.

Two triangles were cut in a Ge foil with different fs-laser parameters. Redeposition structures are visible on the cutting edges, creating residual stresses inside the bulk material. Removing the redeposition structure with a secondary cut using FIB is possible and provides a stress-free state above the edge. To be efficiently used for machining of micro-samples, laser parameters as well as the geometry need to be optimized to avoid redeposition structures or at least to reduce their thickness.

Acknowledgments

We acknowledge synchrotron ESRF for the provision of beamtime allocation at the French beamline BM32-CRG-IF under proposal MA-4958. We thank the BM32 team for their assistance and knowledge during the experiment. We also acknowledge the funding provided by the DFG within the XmicroFatigue project (DFG project number 316,662,945). The authors would like to thank Jean-Baptiste Molin and Konrad Prikoszovich for their help with the experiment.

CRediT authorship contribution statement

R. Fréville: Writing – review & editing, Writing – original draft, Methodology, Investigation, Formal analysis, Data curation. **P.A. Gruber:** Writing – review & editing, Validation, Supervision, Investigation, Conceptualization. **S. Lee:** Writing – review & editing, Data curation, Conceptualization. **J.S. Micha:** Writing – review & editing, Resources, Investigation. **O. Robach:** Writing – review & editing, Resources, Investigation. **O. Ulrich:** Writing – review & editing, Resources, Investigation. **C. Kirchlechner:** Writing – review & editing, Validation, Supervision, Funding acquisition, Conceptualization.

Declaration of competing interest

The authors declare that they have no known competing financial interests or personal relationships that could have appeared to influence the work reported in this paper.

Supplementary materials

Supplementary material associated with this article can be found, in the online version, at doi:10.1016/j.mtla.2025.102648.

References

[1] T. Kim, H.S. Kim, M. Hetterich, D. Jones, J.M. Girkin, E. Bente, M.D. Dawson, Femtosecond laser machining of gallium nitride, Mater. Sci. Eng. B 82 (2001) 262.
[2] H. N, Rizvi and others, femtosecond laser micromachining: current status and applications, Riken Rev 107 (2003).

[3] K.M.T. Ahmmed, C. Grambow, A.M. Kietzig, Fabrication of micro/nano structures on metals by femtosecond laser micromachining, Micromachines 5 (2014) 1219.
[4] B. Tordoff, et al., The LaserFIB: new application opportunities combining a high-performance FIB-SEM with femtosecond laser processing in an integrated second chamber, Appl. Microsc. 50 (2020) 24.
[5] M.J. Pfeifenberger, M. Mangang, S. Wurster, J. Reiser, A. Hohenwarter, W. Pfleging, D. Kiener, R. Pippan, The use of femtosecond laser ablation as a novel tool for rapid micro-mechanical sample preparation, Mater. Des. 121 (2017) 109.
[6] R. Fréville, N. Bruzy, A. Dewaele, Optical full-field strain measurement within a diamond anvil cell, Rev. Sci. Instrum. 94 (2023) 123905.
[7] J. Bonse, J. Krüger, S. Höhm, A. Rosenfeld, Femtosecond laser-induced periodic surface structures, J. Laser Appl. 24 (2012).
[8] E.L. Gurevich, Mechanisms of femtosecond LIPSS formation induced by periodic surface temperature modulation, Appl. Surf. Sci. 374 (2016) 56.
[9] Q. Feng, Y. Picard, H. Liu, S. Yalisove, G. Mourou, T. Pollock, Femtosecond laser micromachining of a single-crystal superalloy, Scr. Mater. 53 (2005) 511.
[10] S. Ma, J. McDonald, B. Tryon, S. Yalisove, T. Pollock, Femtosecond laser ablation regimes in a single-crystal superalloy, Metall. Mater. Trans. A 38 (2007) 2349.
[11] A. Kumar, T.M. Pollock, Mapping of femtosecond laser-induced collateral damage by electron backscatter diffraction, J. Appl. Phys. 110 (2011).
[12] T. Sarnet, J.E. Carey, E. Mazur, From black silicon to photovoltaic cells, using short pulse lasers, in: AIP Conference Proceedings 1464, American Institute of Physics, 2012, pp. 219–228.
[13] E. Coyne, J. Magee, P. Mannion, G. O'connor, T. Glynn, STEM (scanning transmission electron microscopy) analysis of femtosecond laser pulse induced damage to bulk silicon, Appl. Phys. A 81 (2005) 371.
[14] A. Borowiec, M. Mackenzie, G. Weatherly, H. Haugen, Transmission and scanning electron microscopy studies of single femtosecond-laser-pulse ablation of silicon, Appl. Phys. A 76 (2003) 201.
[15] T. Gorelik, M. Will, S. Nolte, A. Tuennermann, U. Glatzel, Transmission electron microscopy studies of femtosecond laser induced modifications in quartz, Appl. Phys. A 76 (2003) 309.
[16] M.P. Echlin, M.S. Titus, M. Straw, P. Gumbsch, T.M. Pollock, Materials response to glancing incidence femtosecond laser ablation, Acta Mater. 124 (2017) 37.
[17] J.G. Gigax, H. Vo, Q. McCulloch, M. Chancey, Y. Wang, S.A. Maloy, N. Li, P. Hosemann, Micropillar compression response of femtosecond laser-cut single crystal Cu and proton irradiated Cu, Scr. Mater. 170 (2019) 145.
[18] L. Borasi, A. Slagter, A. Mortensen, C. Kirchlechner, On the preparation and mechanical testing of nano to micron-scale specimens, Acta Mater (2024) 120394.
[19] C. Kirchlechner, W. Grosinger, M. Kapp, P. Imrich, J.S. Micha, O. Ulrich, J. Keckes, G. Dehm, C. Motz, Investigation of reversible plasticity in a micron-sized, single crystalline copper bending beam by X-ray μ laue diffraction, Philos. Mag. 92 (2012) 3231.
[20] C. Kirchlechner, J. Keckes, J.S. Micha, G. Dehm, In situ μLaue: instrumental setup for the deformation of micron sized samples, Neutrons Synchrotron. Radiat. Eng. Mater. Sci. Fundam. Appl. 425 (2017).
[21] N. Tamura, R. Celestre, A. MacDowell, H. Padmore, R. Spolenak, B. Valek, N. Meier Chang, A. Manceau, J. Patel, Submicron x-ray diffraction and its applications to problems in materials and environmental science, Rev. Sci. Instrum. 73 (2002) 1369.
[22] O. Ulrich, X. Biquard, P. Bleuet, O. Geaymond, P. Gergaud, J.S. Micha, O. Robach, F. Rieutord, A new white beam x-ray microdiffraction setup on the BM32 beamline at the European synchrotron radiation facility, Rev. Sci. Instrum. 82 (2011) 033908.
[23] C. Leclere, T.W. Cornelius, Z. Ren, O. Robach, J.S. Micha, A. Davydok, O. Ulrich, G. Richter, O. Thomas, KB scanning of X-ray beam for Laue microdiffraction on accelero-phobic samples: application to in situ mechanically loaded nanowires, J. Synchrotron. Radiat. 23 (2016) 1395.
[24] J.S. Micha, LaueTools, (2010).
[25] A. Poshadel, P. Dawson, G. Johnson, Assessment of deviatoric lattice strain uncertainty for polychromatic X-ray microdiffraction experiments, J. Synchrotron Radiat. 19 (2012) 237.
[26] J. Petit, M. Bornert, F. Hofmann, O. Robach, J.S. Micha, O. Ulrich, C.L. Bourlot, D. Faurie, A.M. Korsunsky, O. Castelnau, Combining laue microdiffraction and digital image correlation for improved measurements of the elastic strain field with micrometer spatial resolution, Procedia IUTAM 4 (2012) 133.
[27] J. Petit, et al., Laue-DIC: a new method for improved stress field measurements at the micrometer scale, J. Synchrotron Radiat. 22 (2015) 980.
[28] F. Zhang, Determination of the stress field in polycrystalline materials by Laue Microdiffraction, theses, Ecole nationale supérieure d'arts et métiers - ENSAM, 2015.
[29] F.G. Zhang, M. Bornert, J. Petit, O. Castelnau, Accuracy of stress measurement by Laue micro\-diffraction (Laue-DIC method): the influence of image noise, calibration errors and spot number, J. Synchrotron Radiat. 24 (2017) 802.
[30] J. Rethoré, UFreckles, (2018).
[31] W.L. Bond, W.P. Mason, H.J. McSkimin, K.M. Olsen, G.K. Teal, The elastic constants of germanium single crystals, Phys Rev 78 (1950) 176.
[32] R.I. Barabash, G.E. Ice, F.J. Walker, Quantitative microdiffraction from deformed crystals with unpaired dislocations and dislocation walls, J. Appl. Phys. 93 (2003) 1457.
[33] Chapter 79 white beam microdiffraction and dislocations gradients, in: Dislocations in Solids, 13, Elsevier, 2007, pp. 499–601.
[34] E. Chason, J.W. Shin, S.J. Hearne, L.B. Freund, Kinetic model for dependence of thin film stress on growth rate, temperature, and microstructure, J. Appl. Phys. 111 (2012) 083520.
[35] G. Abadias, E. Chason, J. Keckes, M. Sebastiani, G.B. Thompson, E. Barthel, G. L. Doll, C.E. Murray, C.H. Stoessel, L. Martinu, Review article: stress in thin films and coatings: current status, challenges, and prospects, J. Vac. Sci. Technol. A 36 (2018) 020801.
[36] S. Shin, J.K. Park, D.H. Kim, Suppression of spallation induced nanoparticles by high repetition rate femtosecond laser pulses: realization of precise laser material processing with high throughput, Opt. Express 29 (2021) 20545.
[37] R. Zhang, C. Huang, J. Wang, S. Feng, H. Zhu, Evolution of micro/nano-structural arrays on crystalline silicon carbide by femtosecond laser ablation, Mater. Sci. Semicond. Process. 121 (2021) 105299.
[38] C. Florian, Y. Fuentes-Edfuf, E. Skoulas, E. Stratakis, S. Sanchez-Cortes, J. Solis, J. Siegel, Influence of heat accumulation on morphology debris deposition and wetting of LIPSS on steel upon high repetition rate femtosecond pulses irradiation, Materials 15 (2022) 21.
[39] R. Zhang, Q. Wang, Q. Chen, A. Tang, W. Zhao, Experimental study on femtosecond laser processing performance of single-crystal silicon carbide, Appl. Sci. 13 (2023) 13.
[40] S. Shin, Review of high-precision femtosecond laser materials processing for fabricating microstructures: effects of laser parameters on processing quality, ablation efficiency, and microhole shape, J. Laser Appl. 36 (2024) 041201.
[41] M. Meixner, T. Fuss, M. Klaus, M. Genzel, C. Genzel, Diffraction analysis of strongly inhomogeneous residual stress depth distributions by modification of the stress scanning method. II. Experimental implementation, J. Appl. Crystallogr. 48 (2015) 1462.
[42] M. Stefenelli, J. Todt, A. Riedl, W. Ecker, T. Müller, R. Daniel, M. Burghammer, J. Keckes, X-ray analysis of residual stress gradients in TiN coatings by a Laplace space approach and cross-sectional nanodiffraction: a critical comparison, J. Appl. Crystallogr. 46 (2013) 1378.